Multiscale electrical impedance tomography

Marc Pessel and Dominique Gibert
Géosciences Rennes - CNRS/INSU, Université Rennes 1, Rennes, France

Received 25 July 2000; revised 25 November 2001; accepted 30 November 2001; published 29 January 2003.

[1] Electrical impedance tomography aims to recover the electrical conductivity underground from surface and/or borehole apparent resistivity measurements. This is a highly nonlinear inverse problem, and linearized inverse methods are likely to produce solutions corresponding to local minima of the misfit function to minimize. In the present paper, electrical impedance tomography is addressed through a nonlinear approach, namely, simulated annealing, in order to escape from local minima and to produce conductivity distributions independent of the starting models. Simulated annealing belongs to the Monte Carlo family which needs numerous forward modelings, and particular attention is paid both to the forward numerical solution of the Poisson equation and to the parameterization of the inverse problem, i.e., the way the conductivity

with respect to the information content of the data. This is done by means of a multiscale sampling of the conductivity distribution to be recovered. This approach increases the nonlinear nature of the inverse problem since, in practice, we are faced with an inverse problem whose number of parameters increases as the iterative inversion proceeds. However, the computational power now available with desktop computers enables the use of a fully nonlinear approach, namely simulated annealing [*Kirkpatrick et al.*, 1983; *Van Laarhoven and Aarts*, 1987]. This Monte Carlo method is well-suited to tackle the nonlinear nature of the inverse problem by providing possibilities to escape from local minima of the misfit function corresponding to non-optimal solutions. Also, simulated annealing allows a free choice of the misfit function to be minimized, hence preserving the possibility to easily incorporate a priori geological constrains concerning the conductivity distribution to reconstruct.

[3] Section 2 presents the multigrid method used to solve the 2.5-dimensional (2.5-D) forward problem. The efficiency of this method reveals why a multiscale inversion should also be natural. The following section presents the multiscale inversion strategy and its implementation through simulated annealing. The last section contains a field example.

2. Multigrid Forward Modeling

2.1. The 2.5-D Formalism

[4] The 2.5-D approximation needed to invert the data of the field example discussed below is now presented to ensure both the self-consistency of the paper and to illustrate the multiscale solution of the forward problem through the multigrid algorithm. The fundamental equation describing the stationary current flow in the conducting Earth is the Poisson equation [e.g., *Zhdanov and Keller*, 1994]

$$\nabla \cdot (\sigma \nabla \phi) = -I, \tag{1}$$

where ϕ is the electrical potential, σ is the conductivity distribution, and I is the current source term. In the 2.5-D approximation the conductivity distribution is assumed invariant along the horizontal y axis and the source term I restricted to the $y = 0$ vertical plane. The resulting 3-D potential ϕ is thus an even function with respect to y. In this case, equation (1) becomes

$$\nabla \cdot [\sigma(x,z) \nabla \phi(x,y,z)] = -I(x,z)\delta(y). \tag{2}$$

By Fourier transforming this equation in the y direction [*Madden*, 1971; *Pelton et al.*, 1978; *Tripp et al.*, 1984] we obtain a 2-D Poisson equation:

$$\nabla_{xz} \cdot \left[\sigma(x,z) \nabla_{xz} \tilde{\phi}(x,u,z)\right] = -I(x,z) + (2\pi u)^2 \sigma(x,z) \tilde{\phi}(x,u,z) \tag{3}$$

where ∇_{xz} represents the 2-D gradient operator with respect to the x and z variables, u is the dual spatial frequency corresponding to y, and $\tilde{\phi}$ is the Fourier transform of the potential ϕ:

$$\tilde{\phi}(x,u,z) = \int \phi(x,y,z) \exp(-2i\pi u y) dy. \tag{4}$$

For a given frequency u, the additional source term in equation (3) depends on both the frequency and the potential, and is distributed in the whole $y = 0$ plane. This source term corresponds to leaking conductances whose physical sense is to allow the electrical current to flow in the y direction [*Dines and Lytle*, 1981]. The 3-D potential $\phi(x,y,z)$ is obtained by solving the 2-D equation (3) and then inverse Fourier transforming $\tilde{\phi}(x, u, z)$:

$$\phi(x,y,z) = \int \tilde{\phi}(x,u,z) \exp(+2i\pi u y) du. \tag{5}$$

Since the potential electrodes are assumed localized in the $y = 0$ plane, it is sufficient to know the electrical potential in this plane and equation (5) simplifies into

$$\phi(x,0,z) = \int \tilde{\phi}(x,u,z) du. \tag{6}$$

In practice, equation (3) is solved for several discrete frequencies u, and the integral equation (6) is approximated by

$$\phi(x,0,z) = \sum_u \tilde{\phi}(x,u,z), \tag{7}$$

where the sum symbol represents a numerical integration over the variable u which can be done with standard algorithms [*Press et al.*, 1992]. Hopefully, the integration can be accurately performed with a small number of positive discrete spatial frequencies since the Fourier transform $\tilde{\phi}$ is a decreasing exponential-like even function centered on the zero frequency.

2.2. Multigrid Numerical Solution

[5] We use a multigrid algorithm to solve equation (3), a method known to be extremely efficient for numerically

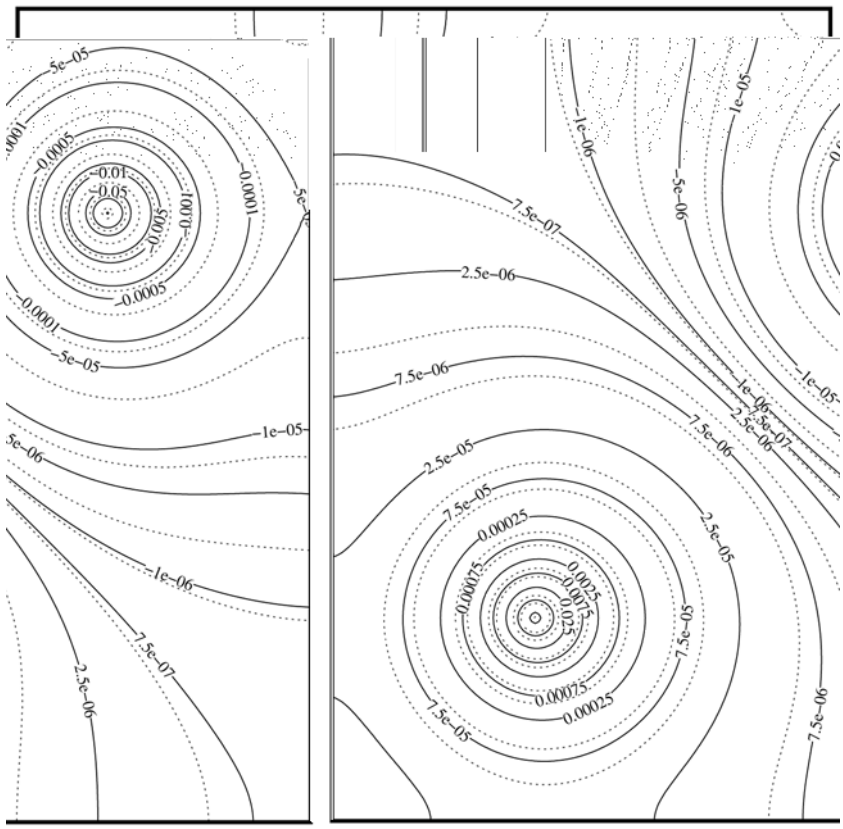

Figure 2. Primary potential obtained for a uniform background with a resistivity of 1.0 Ω m and the same injection electrodes as those in Figure 1.

solving elliptic partial differential equations [*Press et al.*, 1992]. The general principle of multigrid methods is to sequentially construct the solution from coarse grids to finer ones. An approximate low-resolution solution, computed on a coarse grid with a coarse conductivity distribution obtained by both low-pass filtering (moving average) and undersampling the finest conductivity grid is used as a starting solution for the next finer grid. By this way, the algorithm overcomes the well-known slow convergence of classical relaxation methods since the long wavelengths of the potential are first relaxed on the coarsest grids through which the information is more quickly transferred between the grid nodes. As the algorithm proceeds with finer grids, more details of the conductivity distribution are taken into account and small-wavelength features are progressively incorporated into the potential. This is illustrated with a resistivity model (Figure 1) which contains three blocks with different sizes (64, 32, and 16 grid meshes in size and resistivities of 1.5, 100.0, and 0.7 Ω m, respectively) embedded in a uniform background resistivity of 1.0 Ω m. The sequential construction of the potential with the multigrid algorithm is best seen through the secondary potential defined as the difference between the total potential and the potential corresponding to a medium with a constant conductivity (Figure 2). The secondary potentials computed for the successive grid levels are shown in Figure 3, and one can observe that more small-scale details are incorporated into the solution as the algorithm proceeds from the coarsest 8 × 8 grid (Figure 3a) to the finest 256 × 256 grid (Figure 3f).

3. Multiscale Inversion With Simulated Annealing

3.1. Adaptive Multiscale Parameterization

[6] We now address the recovery of the conductivity distribution from potential measurements. This is a nonlinear inverse problem whose ill-posedness arises from both underdetermination (i.e., less data than model parameters) and incomplete data coverage [e.g., *Kohn and Vogelius*, 1984; *Breckon and Pidcock*, 1987; *Li and Oldenburg*, 1992]. The latter point is best seen by recasting Poisson equation (1) as an integral equation [e.g., *Snyder*, 1976]. The potential ϕ induced by a current point source located at point r_i and measured at point r_m is then given by

$$\phi(r_m|r_i) = \frac{I(r_i)}{2\pi\sigma(r_i)|r_i - r_m|} + \int_V \frac{\nabla \ln\sigma(r)\cdot\nabla\phi(r|r_i)}{2\pi|r - r_m|}\,dv, \quad (8)$$

where I is the current injected at point r_i and V is the lower half-space including the whole conducting ground. The first right-hand term of equation (8) is the primary potential of the injection electrode which provides no information about the conductivity distribution σ excepted at point r_i. Indeed, the primary potential is the one obtained for a uniform medium with a conductivity σ (r_i) (Figure 2).

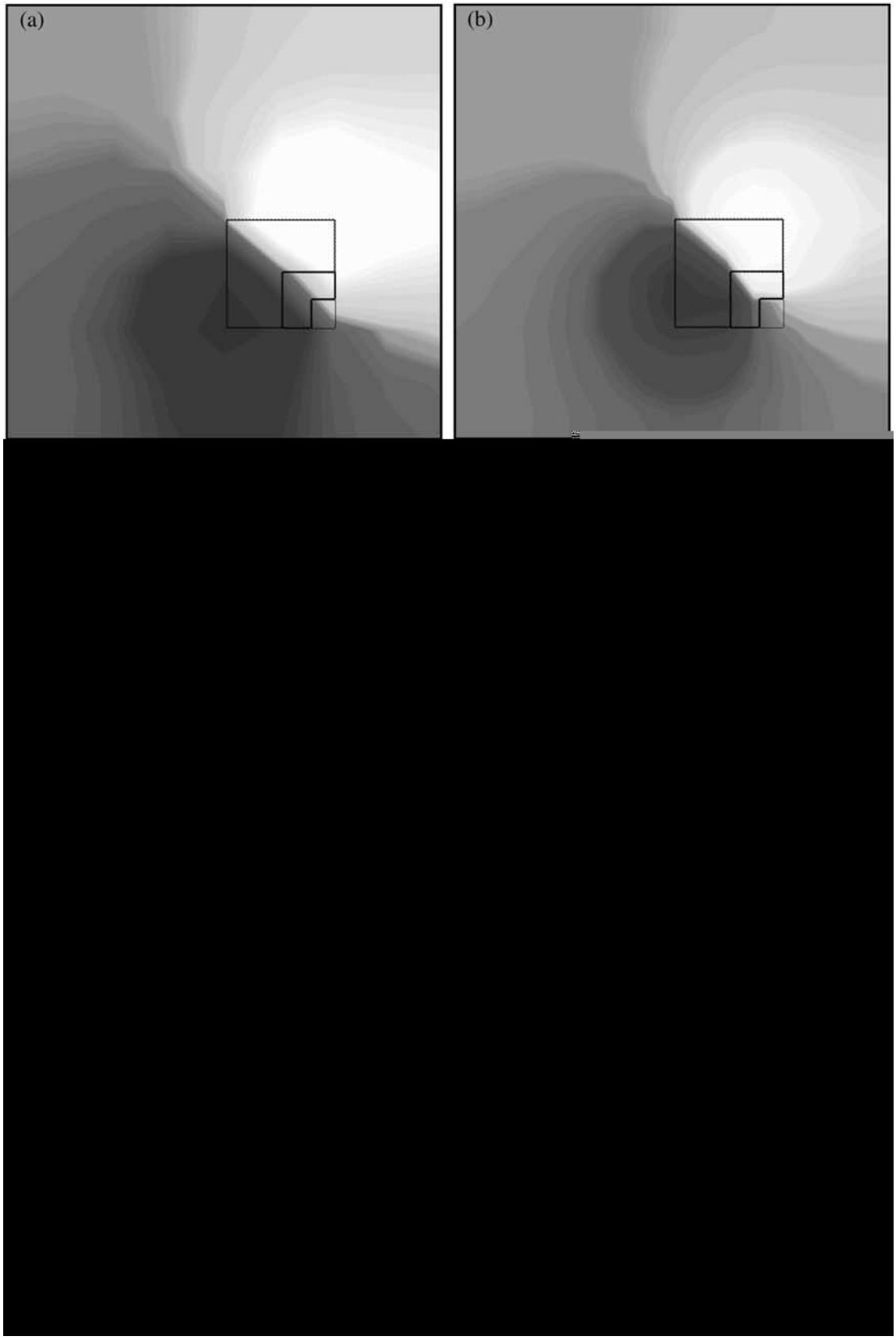
(a)
(b)

Information concerning the conductivity distribution is brought by the integral in equation (8) which represents the secondary potential created by the volumetric charge density,

$$Q(r|r_i) = 2\varepsilon_o \nabla \ln \sigma(r) \cdot \nabla \phi(r|r_i), \tag{9}$$

which depends on the potential ϕ whose characteristics are controlled by both the conductivity distribution σ and the point r_i, where the current is injected. A high charge density Q exists at sharp conductivity gradients on the edges of the conducting bodies provided that a significant component of the electrical current is parallel to the conductivity gradient. This can be observed in Figure 3 where the secondary potential has extrema only where the current vectors are almost orthogonal to the edges of the blocks (Figure 4). Hence multiple current sources must be used to correctly image a block in order to guarantee that current vectors cross all boundaries [*Li and Oldenburg*, 1992]. The integral formulation of the direct problem given in equation (8) shows that the fundamental quantity to be inverted is $\ln \sigma$. This makes the inversion invariant (except for the sign) with respect to a model parameterization in term of either conductivity or resistivity.

[7] The underdetermination of the inverse problem may be partly controlled by the particular parameterization used to represent the unknown conductivity distribution. In the present study we adopt a compact paving with blocks V_k such that the half-space

$$V = \bigcup_k V_k \tag{10}$$

with

$$V_i \bigcap V_{j \neq i} = \emptyset, \tag{11}$$

and equation (8) may be rewritten as

$$\phi(r_m|r_i) = \frac{I(r_i)}{2\pi\sigma(r_i)|r_i - r_m|} + \sum_k \int_{V_k} \frac{\nabla \ln \sigma(r) \cdot \nabla \phi(r|r_i)}{2\pi|r - r_m|} dv, \tag{12}$$

Blocks where either no sharp conductivity gradient exists or no well-oriented electrical current flows correspond to almost vanishing integrals in equation (12), and underdetermined quantities appear in the nonlinear system of equations to be solved. An optimal representation of the conductivity distribution should be such that every block V_k has a significant integral with respect to the data. This regularizes the inverse problem by reducing both its condition number and the number of unknown parameters [e.g., *Yorkey*, 1990] but also makes the inverse problem more complicated because the optimal block decomposition depends on the conductivity distribution determined during the inversion.

[8] In the present paper, the distribution $\ln \sigma$ is represented by irregular cells of constant conductivity obtained by clustering adjacent meshes of the finest grid used to describe the conductivity distribution in the multigrid forward problem. This allows an optimal fitting to oblique multiscale structures like the one shown on Figure 5, and this multiscale approach is able to describe complex conductivity distributions with a small number of parameters since small-size cells are placed only where small-scale variations in the conductivity exist [e.g., *Mehrabi and Sahimi*, 1997].

3.2. Sensitivity Analysis and Grid Refinement

[9] In practice, the multiscale block decomposition of the conductivity model is constructed while the inversion progresses by first searching for a coarse block decomposition of the conductivity and progressively includes finer blocks in the model (Figure 6). Let us suppose that the inversion presently deals with a given block decomposition for which the optimal conductivity has been obtained, i.e., the minimum of the misfit function (defined as either the L_1 or L_2 norm in the present study) has been reached. The next step is to decide if a refinement of the block model is desirable to eventually further reduce the misfit. Addressing this problem by comparing the decrease of the misfit against the price paid by adding parameters in the model is time consuming since this needs to solve the refined model to apply the decision criteria. In order to save computer time we instead performed a prior sensitivity analysis [*McGillivary and Oldenburg*, 1990] to determine whether or not a given block refinement is significant.

[10] Let the current conductivity model with K blocks issued from the last step of the inversion process be

$$m_l = \{b_1, \cdots b_k, \cdots b_K | \sigma_1, \cdots \sigma_k, \cdots \sigma_K\}, \tag{13}$$

where the b_k represent the blocks and σ_k represent their conductivities. In practice, each block is identified by a particular flag k attributed to a set of meshes belonging to the finest conductivity grid used in the multigrid forward problem. All meshes sharing a common flag have the same conductivity and constitute a single block in the model. Our strategy for model refinement is to sequentially consider each block b_k as a candidate for refinement by subdividing it into four $\{b_{k,1}, b_{k,2}, b_{k,3}, b_{k,4}\}$ subblocks whose conductivities $\{\sigma_{k,1}, \sigma_{k,2}, \sigma_{k,3}, \sigma_{k,4}\}$ are to be determined in the subsequent inversion steps. Once the splitting of block b_k has been realized, a sensitivity analysis is performed by successively assigning a conductivity $\sigma_{k,i} = \sigma_k + \delta\sigma$ to each subblock while the other three blocks are held constant. The solutions of the forward problems corresponding to these new conductivity models give an insight of their influence on the data, and if a significant influence is found for at least one new subblock, the

Figure 3. (opposite) Graphs of the secondary electrical potential solutions obtained at successive grid levels for the multigrid forward problem corresponding to the conductivity model shown in Figure 1. The grid sizes are 8^2, 16^2, 32^2, 64^2, 128^2, and 256^2 for Figures 3a to 3f, respectively. The secondary potential is defined as the total potential minus the potential corresponding to a uniform model with the background resistivity (1.0 Ω m). As the grid mesh becomes finer (i.e., the grid size increases), more and more small-scale details appear in the potential (negative and positive values are in black and white, respectively).

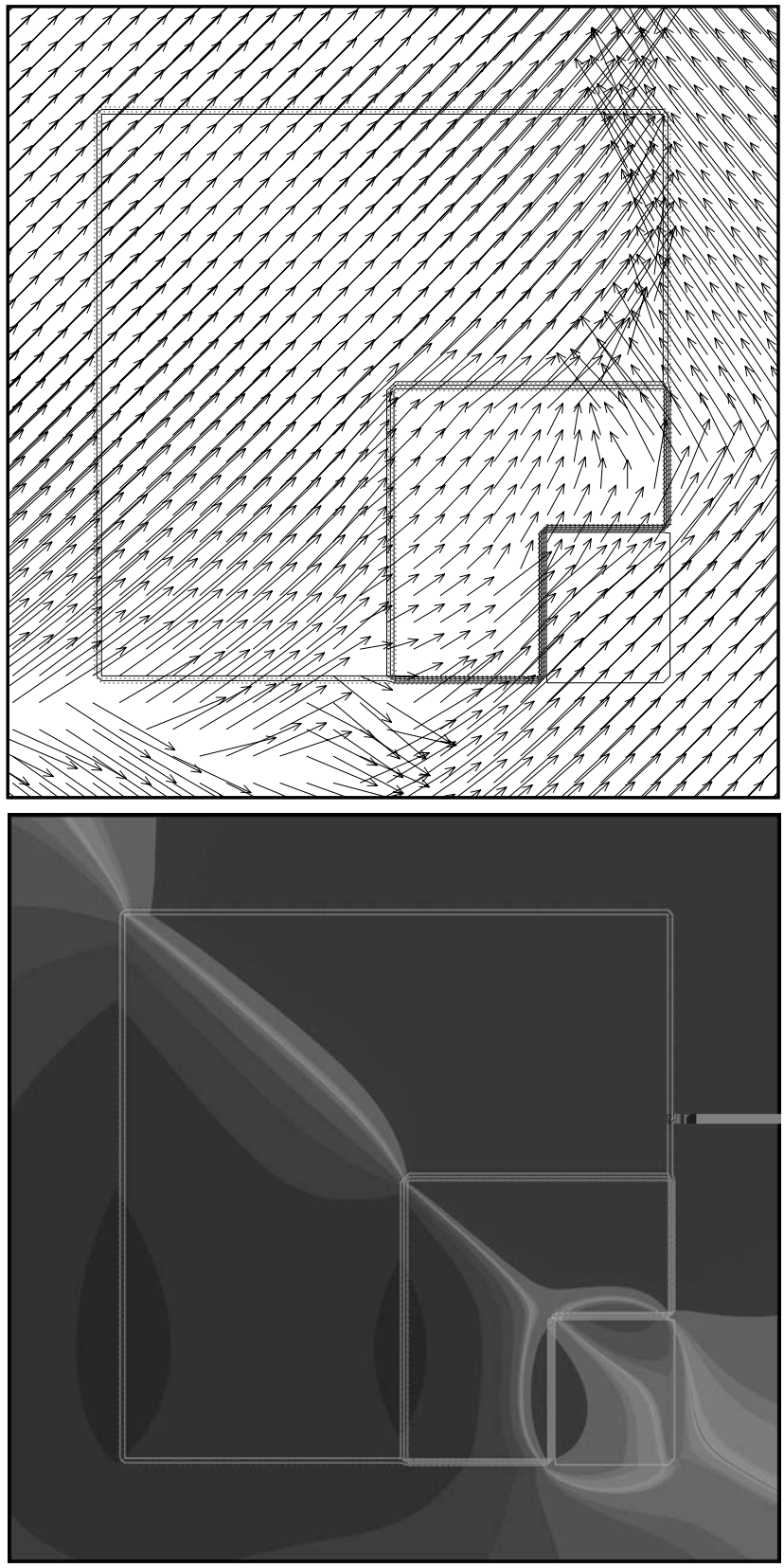

Figure 4. (top) Flow lines of the electrical current crossing the resistivity structure shown in Figure 1. (bottom) Secondary potential (zoomed from Figure 3f) with extrema located where the electrical current flows almost perpendicularly to an edge, and where the charge accumulation is maximum.

subdivision of block b_k is kept and the conductivities of the newly created four subblocks are a priori determined through a linearized inversion. The refinement procedure replaces the current conductivity model by one with more small blocks and induces changes in the conductivities of adjacent nonrefined blocks. In practice we observed that in many situations the conductivities are correctly re-estimated only when a full nonlinear inversion method is used. We chose a simulated annealing approach for the inversion which we found efficient in previous studies [*Gibert and Virieux*, 1991; *Gibert et al.*, 1994; *Courboulex et al.*, 1996].

3.3. Simulated Annealing

[11] Simulated annealing is a stochastic nonlinear algorithm well adapted to solve the present inverse problem whose misfit function may possess local minima. Also, simulated annealing is a flexible method which allows a free choice of the misfit function and an easy account of a priori information concerning the conductivity distribution to reconstruct [*Kirkpatrick et al.*, 1983; *Cerny*, 1985; *Van Laarhoven and Aarts*, 1987; *Tarantola*, 1987]. The basic principle of simulated annealing is to iteratively modify the model until it converges toward the minimum of the misfit function to be minimized. In order to keep a memory in the sequence of models generated during the iterations, the model created at iteration l is obtained by perturbing the previous model in the sequence

$$m_l = m_{l-1} + \delta_{ml}, \tag{14}$$

where the random perturbation δm_l must be such that an importance sampling of the a priori distribution of the models is guaranteed. Once model m_l is created, its posterior probability $p(m_l)$ is computed in order to decide whether or not m_l is to be kept in the sequence of models. The acceptance probability of the transition from model m_{l-1} to model m_l is given by

$$p_T(m_{l-1} \rightarrow m_l) = \min\left[1, \left(\frac{p(m_l)}{p(m_{l-1})}\right)^{1/T}\right], \tag{15}$$

where T is a positive parameter called the temperature [*Kirkpatrick et al.*, 1983]. When the probability of the new model is worse than the previous one the transition is not

where C is a normalization constant. At $T = 1$, $p_{T=1}(m_l) = p(m_l)$, and the Metropolis algorithm then performs an importance sampling in the sense that the sampling density of the models into the a priori space equals the a posteriori probability density of the models. Simulated annealing loops over the Metropolis algorithm while the temperature decreases in order to guide the sampling toward the region where the posterior probability is maximum. Assuming that the starting temperature may be considered infinite, the probability equation (16) is uniform and any model belonging to the a priori space is accepted. As the temperature decreases, the probability equation (16) becomes irregular with maxima and minima, and the accepted models concentrate near the maxima. Finally, when $T \downarrow 0$, the probability is reduced to a Dirac δ function located at the best model:

$$p_{T\downarrow 0}(m_l) = \delta(m_l - m_{\text{best}}). \tag{17}$$

[12] An important aspect of simulated annealing is to properly design the cooling schedule which controls the efficiency of the guidance toward the maxima of the a posteriori probability. A common guideline is to decrease the temperature sufficiently slowly so that the importance sampling gently diffuses and concentrates around the maximum of the posterior probability [*Van Laarhoven and Aarts*, 1987]. Another important issue of simulated annealing is to define the model-generation process equation (14) in order to properly sample the a priori space of models. In the present study, the only a priori constraints we applied are hard bounds on the conductivity values.

3.4. Synthetic Example

[13] We now illustrate the whole inversion procedure with a simple synthetic example where the conductivity distribution to recover is shown in Figure 7. It can be seen that this structure is multiscale and possesses both large homogeneous areas and small-scale heterogeneities. The synthetic data have been generated with the multigrid forward problem discussed above. Five pairs of injection electrodes are placed on both lateral sides and on the top side of the model, and all other electrodes are potential electrodes. The data set then consists of $15 \times 94 = 1410$ potential values. In order to assess for the capability of our resampling algorithm to correctly adjust to the structure to be recovered, no noise was added to the synthetic data. The particular choice of a posterior probability distribution for the data residuals is therefore meaningless and, in the present example, we use a normal Gaussian distribution with unit variance (i.e., an L_2 misfit function). The inversion begins with a single-block model whose conductivity is determined through a quick annealing sequence. Figure 7 shows the best models obtained during a four-step resampling sequence where the smallest allowed block size varies from 1/2 to 1/16 unit length. The final first level solution (Figure 7a), issued from the zero level (with a single block), counts 4 blocks with differing conductivities. As can be seen, this coarse model already reproduces the large-scale structure of the synthetic model. The second level solution (Figure 7b) has been partly resampled and the upper right block of the first level model has been preserved. Interestingly, we observe that the resampling has been automatically restricted in an area containing the small scale heterogeneities of the synthetic model. As a consequence, the second level solution only counts 13 blocks instead of 16 if a full resampling of the first level solution had been performed. The next third and fourth levels further refine

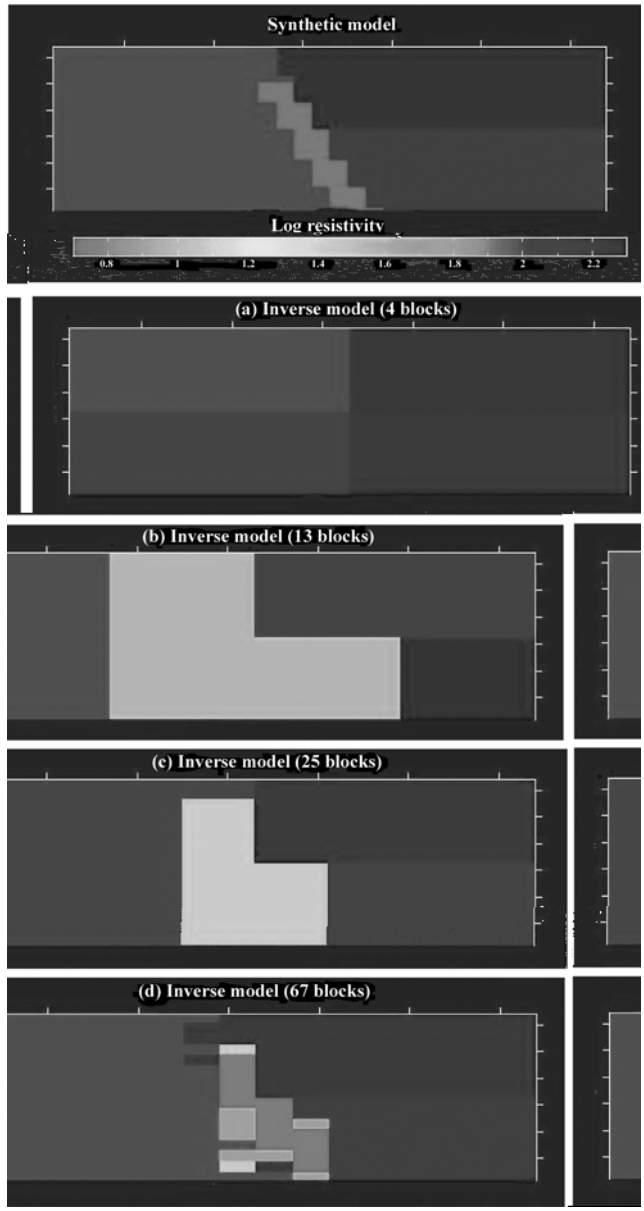

Figure 7. Resistivity model used to produce the synthetic data of the synthetic example. The resistivity distribution possesses both large-scale and small-scale features. (a–d) Solutions obtained at the end of each inversion of a four-step resampling sequence applied to the synthetic data corresponding to the synthetic model shown at the top of the figure. At the beginning of each step of the resampling sequence, a sensitivity analysis is performed to identify the blocks which have to be divided into four equal-sized subblocks. A simulated annealing inversion follows to obtain the conductivity distribution corresponding to this new parameterization. It can be seen that the resampling automatically restricts itself to areas where the actual conductivity model possesses small-scale features.

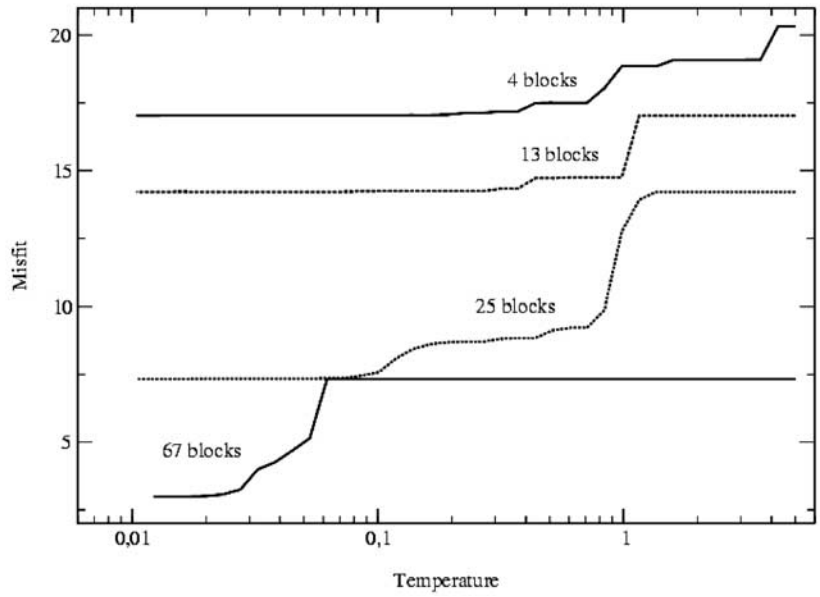

Figure 8. Cooling series of the four-step resampling sequence corresponding to the solutions shown in Figure 7. The misfit displayed corresponds to the best model presents in the simplex at a given temperature. For each step corresponding to a given parameterization of the conductivity model, the misfit displays a sharp decrease corresponding to the convergence toward an optimal solution before the misfit remains constant when the temperature continues to decrease. A further decrease of the misfit is obtained after each resampling step which allows the conductivity distribution to possess finer and finer details.

the solution around the small scale features while remaining coarse scaled elsewhere. This results in solutions with a reduced number of parameters (i.e., blocks) since the final fourth level solution only counts 67 blocks instead of the 256 blocks of the fully resampled grid.

[14] Figure 8 shows the evolution of the misfit (here the sum of squared residuals) during the inversion process which consists in four successive simulated annealing sequences. The misfit for the first level solution with four blocks (Figure 8) indicates a global decrease as the annealing temperature decreases from 5 to 0.01. The step-like nature of the misfit curve reveals the existence of several critical temperatures and is observed when a hierarchical order exists among the parameters of the inverted model [e.g., *Gibert and Virieux*, 1991]. In the present instance, the hierarchy comes from the fact that the synthetic data are very sensitive to the shallowest blocks of the model. Consequently, the simulated annealing inversion first adjusts the conductivity of these blocks, producing the first step-like decrease of the misfit near $T = 4$ and then refines the solution by adjusting the conductivity of the entire model, producing the second main step in the misfit curve near $T = 1$. No further significant improvement is observed at lower temperatures, and the process could have been stopped at $T = 0.1$. The other three inversions also start at $T = 5$ because the sequence of models generated at high temperature performs a global sampling of the model space and allows it to escape from possible local minima of the misfit function. Observe that each resampling allows a further decrease of the misfit with respect to the final value obtained at the end of the preceding inversion. For comparison, downhill simplex inversions with the same 67 blocks model always produced solutions with a much larger misfit than obtained with annealing.

4. Inversion of the Pont-Péan Data

4.1. Geological Context and Field Operations

[15] The Pont-Péan mining site corresponds to a dioritic mineralized dike which has been intensively prospected and exploited during the 18th and 19th centuries until a massive flood invaded the galleries in April 1904 and definitely halted mining. The dike is approximately 15 m thick, 4 km long, and almost north-south oriented with a 80° eastward inclination. The dike, which has been dug down to 600 m in-depth, is located in a fault plane separating Precambrian schist on the western side from Tertiary sediments on the eastern side. The thickness of the Tertiary sediments is about 80 m at the locus of the electrical profile.

[16] The electrical resistivity survey was performed with a 64-electrode pole-dipole array (315 m in length and electrode spacing of 5 m). For practical reasons, the pole-dipole survey was not symmetrical and all measurements were acquired with the remote current electrode located 1000 m westward. For most data, the relative signal-to-noise ratio is greater than 99% with smaller values for only a limited number of measurements corresponding to poor electrode contacts. The pole-dipole pseudo-resistivity section constructed with 360 measurements is shown in Figure 9d and displays low apparent resistivities on the eastern side in rough accordance with the known geological structure of the site. The fact that all data were acquired with the remote electrode kept on the western side of the profile produces a bias of the apparent resistivities toward the true resistivity of

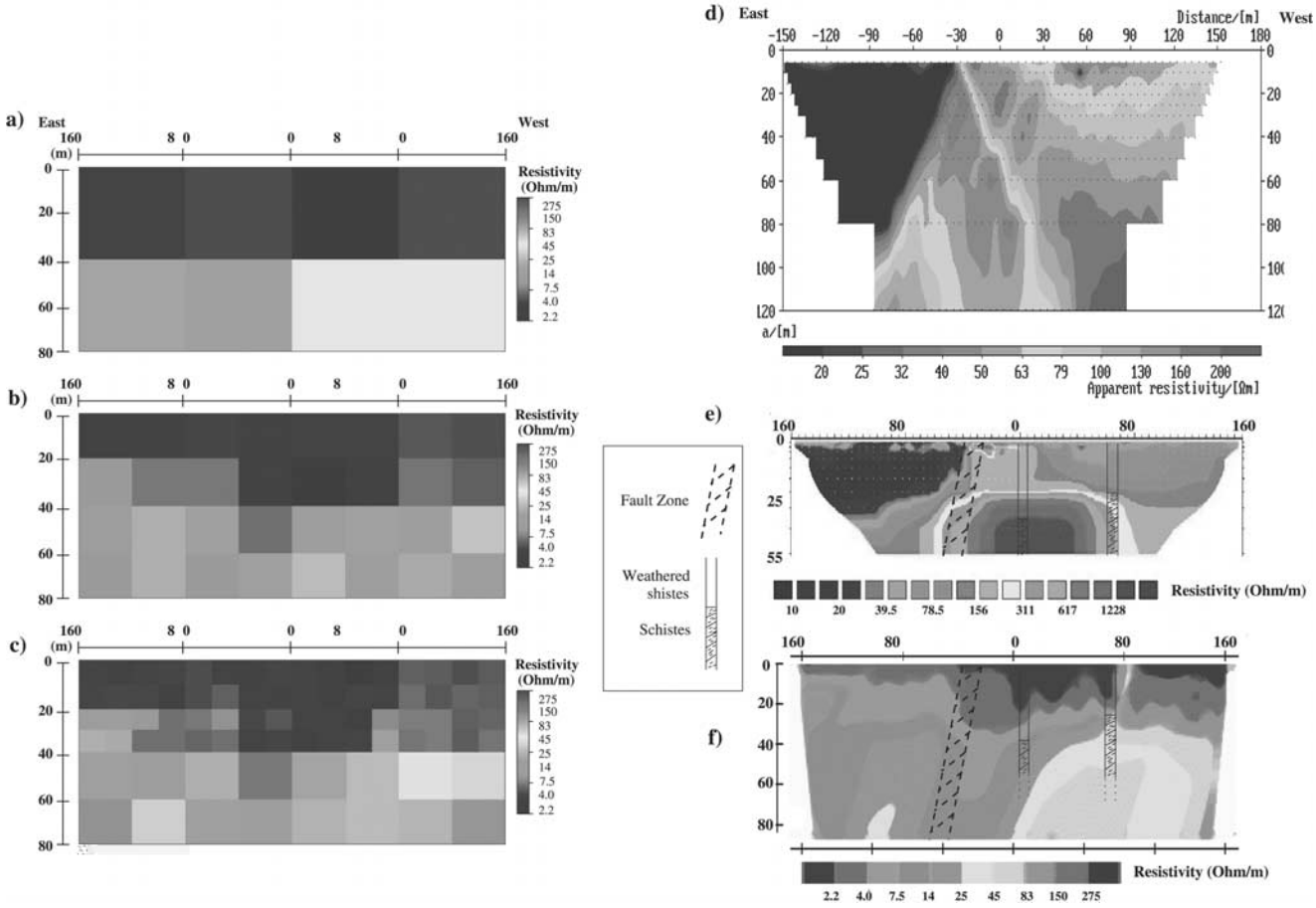

Figure 9. Resistivity models obtained at the end of each stage of the inversion of the pole-dipole data for the (a) 4 × 2 coarse final model, (b) 8 × 4 resampled final model, and (c) final 80-block model obtained from a partial resampling of the top part of the 8 × 4 model. This allowed a refinement of the conductivity distribution in the shallowest part of the model and was accompanied by an additional slight decrease of the misfit function (see Figure 10). The geological information available is shown: the fault location coincides with a low-resistivity dipping zone and the thickness of the low-resistivity zone located immediately westward of the fault agrees with the weathered schists found in two boreholes (B1 and B2). (d) Data obtained for the pole-dipole array and arranged in a pseudo-section of the logarithm of the apparent resistivity. The remote electrode is 1000 m westward, i.e., on the right of the profile. The dike is approximately located at $x = -30$ m. Since the remote electrode is on the resistive right part of the profile, the apparent resistivities are biased toward the high values. (e) Resistivity model obtained by inverting the data with the RES2DINV software by *Loke and Barker* [1996]. (f) Smoothed version of the resistivity section shown in Figure 9c.

the western part of the profile [*Ward*, 1990]. However, the apparent-resistivity section is typical of the one expected for a two-block structure with a nearly vertical fault plane located at $x = -30$ m.

4.2. Inversion

[17] The inversion of the Pont-Péan data follows the same steps as those performed for the synthetic example. However, in order to account for eventual outliers in the data set, a Cauchy distribution (i.e., a L_1 norm) is retained for the probability distribution of the data residuals. Also, in order to reduce the number of forward modelings the data corresponding to the shallowest penetration depths have not been used. The inversion starts with a coarse 4 × 2 blocks model (Figure 9a) which already displays a conductivity distribution corresponding to the expected geological structure with a more resistive part on the west side. The L_1 misfit (Figure 10) decreases by more than one order of magnitude during this first step of the inversion. During the next step of the inversion, the coarse 4 × 2 model is fully re-sampled into the 8 × 4 blocks model shown in Figure 9b. This latter model further refines the conductivity distribution determined during the first step of the inversion, particularly in the middle of the profile near the fault location and reduces the misfit by one more order of magnitude. The sharp increase of the misfit observed at the very beginning of this stage of the inversion indicates that a reannealing operates and incorporates high-misfit models into the simplex which, for this step, counts 33 models. This permits a global rearrangement of the conductivity distribution to escape from the local misfit minimum reached during the previous step of the inversion. The

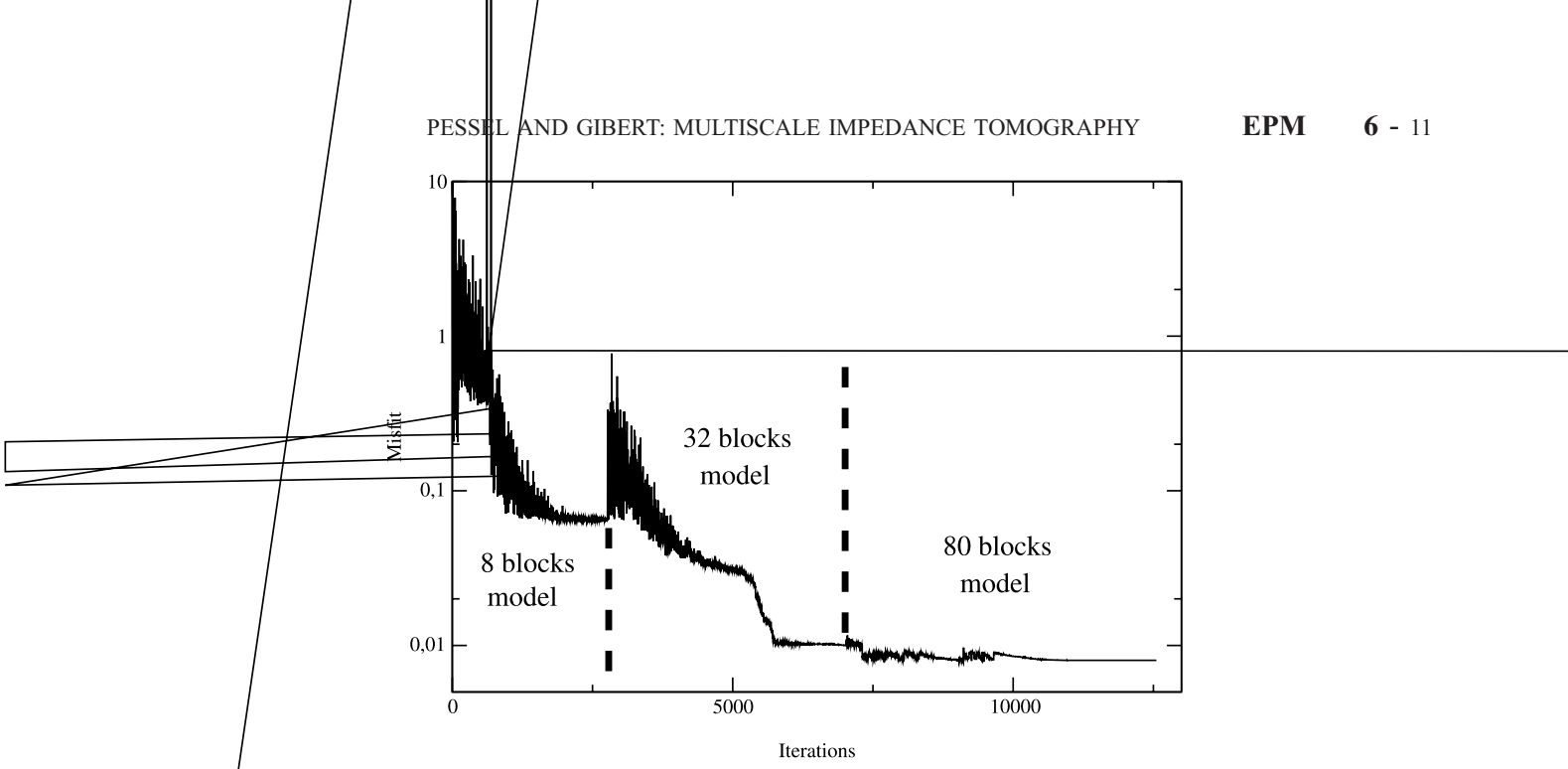

Figure 10. Evolution of the misfit of the models accepted by the Metropolis test during the simulated annealing inversion. Each resampling is associated with a sudden increase of the misfit indicating a reannealing which allows convergence at a lower misfit than the best one obtained with the previous coarser model.

last step of the inversion is done with a resampling restricted to the upper half part of the previous 8 × 4 block model leading to a total of 80 blocks. This allows a refinement of the conductivity distribution in the shallowest part of the structure (Figure 9c) accompanied by slight changes in the lower part of the conductivity distribution. This last step of the inversion process produces only a decrease of the misfit by a factor of 2.

4.3. Discussion

[18] Although the present paper is not devoted to the geological interpretation of the Pont-Péan mining area, the results obtained from the inversion discussed above deserve several comments since geological information is available to assess for the inversion results. In particular, the position of the dike is known, and two boreholes performed in 1958, 400 m southward from the resistivity survey, and located 40 m and 100 m westward of the fault indicate highly weathered schist over thicknesses of 35 m and 25 m, respectively. Figure 9f shows the final resistivity model which appears in very good agreement with the geological information available. Historical data indicate that both the dioritic dike and the schist just beneath are very fractured with an important water circulation (the mining industry suddenly ceased on 4 April 1904, after the galleries were invaded by a huge deep water flood), and may constitute an hydrological sink draining the water and explaining the cone-like geometry of the weathered schist layer. At this stage of the discussion, it must be said that our inversions were performed in a blind manner, i.e., without knowing both the exact location of the fault and the existence of the two boreholes. The reviewers asked us to compare our inversion with other popular algorithms, and we inverted our data (R. Ruault, personal communication, 2001) with the RES2DINV linearized software using the same L_1 norm as for our inversion [*Loke and Barker*, 1996]. The resulting resistivity model (Figure 9e) spans a smaller depth range than for our inversion and is only comparable to the upper part of our model (Figure 9f). Both models are globally coherent with higher conductivities in the eastern half of the models. However, the conductivity distribution recovered with the linearized inversion fails at producing a model in accordance with the geological constraints available in the fault zone. In particular, the conductive area corresponding to the weathered schist observed in the boreholes is not well recovered. This discrepancy may be due to a trapping of the linearized solution in a local minimum of the misfit function. Conversely, it seems that the nonlinear inversion is able to escape from local minima and converges toward a more realistic model.

5. Conclusion

[19] The multiscale formulation of the conductivity inverse problem presented in this paper has been designed to account for both the multiscale nature of the geological structures and the ill-posedness of the inverse problem. This is done through a sequence of inversions where small-scale details are progressively incorporated into the conductivity model. The adaptative multiscaling is controlled by a prior sensitivity analysis which identifies the regions where a resampling is necessary. The sequential multiscale inversion must be treated in a fully nonlinear way in order to enable the rescaled models to escape from local maxima of the a posteriori probability distribution. Simulated annealing appears efficient in this respect and other related nonlinear methods like genetic algorithms may equivalently be used. A synthetic example shows that the multiscale formulation is able to automatically adapt itself to the multiscale geometry of the structure to be recovered although the decision test used in the present study consists in a simple

threshold criteria. More sophisticated criteria should probably be designed in more complex situations. An application to real data obtained over the faulted structure of a mining area allows for an assessment of the method. On the overall, the multiscale nonlinear approach presented in this paper, although deserving further improvements and tests, already appears useful to produce optimally designed models according to the data available. This constitutes a way to give a practical insight to the resolution achieved which, for the problem of electrical resistivity tomography, appears highly nonstationary.

[20] **Acknowledgments.** We thank the Galène association (pontpean.le-village.com/galene) for providing us with both geological and historical information concerning the mining industry of Pont-Péan. Georges Ruelloux offered kind and efficient assistance during the field operations. René Ruault performed the inversion with the RES2DINV software. One anonymous Associate Editor and a referee made very constructive comments that greatly improved the manuscript. This work is financially supported by the CNRS and ANDRA through the GdR FORPRO (Research action 99.II) and is GdR FORPRO contribution 2000/33A. This study is a part of the Electrical Tomography Project of the CNRS ACI Eau et Environnement.

References

Allers, A., and F. Santosa, Stability and resolution analysis of a linearized problem in electrical impedance tomography, *Inverse Probl.*, *7*, 515–533, 1991.

Asch, T., and H. F. Morrison, Mapping and monitoring electrical resistivity with surface and subsurface electrode arrays, *Geophysics*, *54*, 235–244, 1989.

Berryman, J. G., and R. V. Kohn, Variational constraints for electrical-impedance tomography, *Phys. Rev. Lett.*, *65*, 325–328, 1990.

Bevc, D., and H. F. Morrison, Borehole-to-surface electrical resistivity monitoring of a salt water injection experiment, *Geophysics*, *56*, 769–777, 1991.

Borcea, L., J. G. Berryman, and G. C. Papanicolaou, Matching pursuit for imaging high-contrast conductivity, *Inverse Probl.*, *15*, 811–849, 1999.

Breckon, W. R., and M. K. Pidcock, Mathematical aspects of impedance imaging, *Clin. Phys. Physiol. Meas.*, *8*, 77–84, 1987.

Cerny, V., A thermodynamic approach to the travelling salesman problem, *J. Optim. Theory Appl.*, *45*, 41–51, 1985.

Cherkaeva, E., and A. Tripp, Inverse conductivity problem for noisy measurements, *Inverse Probl.*, *12*, 869–883, 1996.

Courboulex, F., J. Virieux, and D. Gibert, On the use of simulated annealing method and cross-validation theory for deconvolution of seismograms, *Bull. Seismol. Soc. Am.*, *86*, 1187–1193, 1996.

Daily, W., and A. Ramirez, Electrical imaging of engineered hydraulic barriers, *Geophysics*, *65*, 83–94, 2000.

Daily, W., A. Ramirez, D. LaBrecque, and J. Nitao, Electrical resistivity tomography of vadose water movement, *Water Resour. Res.*, *28*, 1429–1442, 1992.

Dines, K., and R. Lytle, Analysis of electrical conductivity imaging, *Geophysics*, *46*, 1025–1036, 1981.

Ellis, R. G., and D. W. Oldenburg, Applied geophysical inversion, *Geophys. J. Int.*, *116*, 5–11, 1994a.

Ellis, R. G., and D. W. Oldenburg, The pole-pole 3-D DC-resistivity inverse problem: A conjugate gradient approach, *Geophys. J. Int.*, *119*, 187–194, 1994b.

Gibert, D., and J. Virieux, Electromagnetic imaging and simulated annealing, *J. Geophys. Res.*, *96*, 8057–8067, 1991.

Gibert, D., B. Tournerie, and J. Virieux, Superresolution electromagnetic imaging of the conductive Earth's interior, *Inverse Probl.*, *10*, 341–351, 1994.

Hagrey, S. A., and J. Michaelsen, Resistivity and percolation study of preferential flow in vadose zone at Bokhorst, Germany, *Geophysics*, *64*, 746–753, 1999.

Kirkpatrick, S., C. D. Gelatt, and M. P. Vecchi, Optimization by simulated annealing, *Science*, *220*, 671–680, 1983.

Kohn, R. V., and M. Vogelius, Determining the conductivity by boundary measurements, *Commun. Pure Appl. Math*, *37*, 289–298, 1984.

Li, Y., and D. W. Oldenburg, Approximate inverse mapping in DC resistivity problems, *Geophys. J. Int.*, *109*, 343–362, 1992.

Li, Y., and D. W. Oldenburg, Inversion of 3-D DC resistivity data using an approximate inverse mapping, *Geophys. J. Int.*, *116*, 527–537, 1994.

Li, Y., and D. W. Oldenburg, 3-D inversion of induced polarisation data, *Geophysics*, *65*, 1931–1945, 2000.

Loke, M. H., and R. D. Barker, Rapid least squares inversion of apparent resistivity pseudosections using a quasi-Newton method, *Geophys. Prospect.*, *44*, 131–152, 1996.

Madden, T., The resolving power of geoelectric measurements for delineating resistive zones within the crust, *The Structure and Physical Properties of the Earth's Crust, Geophys. Monogr. Ser.*, vol. 14, edited by J. G. Heacock, pp. 95–105, AGU, Washington, D.C., 1971.

McGillivary, P. R., and D. W. Oldenburg, Methods for calculating Fréchet derivatives and sensitivities for nonlinear inverse problems: A comparative study, *Geophys. Prospect.*, *38*, 499–524, 1990.

Mehrabi, A. R., and M. Sahimi, Coarsening of heterogeneous media: Application of wavelets, *Phys. Rev. Lett.*, *79*, 4385–4388, 1997.

Metropolis, N., A. Rosenbluth, N. Rosenbluth, A. Teller, and E. Teller, Equation of state calculations by fast computing machines, *J. Chem. Phys.*, *21*, 1087–1092, 1953.

Molyneux, J. E., and A. Witten, Impedance tomography: Imaging algorithms for geophysical applications, *Inverse Probl.*, *10*, 655–667, 1994.

Moosegaard, K., and A. Tarantola, Monte-Carlo sampling of solutions of inverse problems, *J. Geophys. Res.*, *100*, 12431–12447, 1995.

Nowroozi, A. A., S. B. Horrocks, and P. Henderson, Saltwater intrusion into the freshwater aquifer in the eastern shore of Virginia: A reconnaissance electrical resistivity survey, *J. Appl. Geophys.*, *42*, 1–22, 1999.

Park, S., Fluid migration in the vadose zone from 3-D inversion of resistivity monitoring data, *Geophysics*, *63*, 41–51, 1998.

Pelton, W., L. Rijo, and C. Swift, Inversion of two-dimensional resistivity and induced-polarization data, *Geophysics*, *43*, 788–803, 1978.

Press, W. H., S. A. Teukolsky, W. K. Vetterling, and B. P. Flannery, Numerical Recipes in FORTRAN 77, 966 pp., Cambridge Univ. Press, New York, 1992.

Ramirez, A., W. Daily, D. LaBrecque, E. Owen, and D. Chesnut, Monitoring an underground steam injection process using electrical resistance tomography, *Water Resour. Res.*, *29*, 73–87, 1993.

Snyder, D. D., A method for modeling the resistivity and IP responses of two-dimensional bodies, *Geophysics*, *41*, 997–1015, 1976.

Spies, B. R., and R. G. Ellis, Cross-borehole resistivity tomography of a pilot-scale, in-situ vitrification test, *Geophysics*, *60*, 886–898, 1995.

Tarantola, A., Inverse Problem Theory, Elsevier Sci., New York, 1987.

Torres-Verdin, C., V. L. Druskin, S. Fang, L. A. Knizhnerman, and A. Malinverno, A dual-grid nonlinear inversion technique with applications to the interpretation of dc resistivity data, *Geophysics*, *65*, 1733–1745, 2000.

Tripp, A., G. Hohmann, and C. Swift, Two-dimensional resistivity inversion, *Geophysics*, *49*, 708–717, 1984.

Van, G. P., S. K. Park, and P. Hamilton, Monitoring leaks from storage ponds using resistivity methods, *Geophysics*, *56*, 1267–1270, 1991.

Van Laarhoven, P. J. M., and E. H. C. Aarts, Simulated Annealing: Theory and Applications, Reidel, D., Norwell, Mass., 1987.

Ward, S. H., Resistivity and induced polarization methods, in *Geotechnical and Environmental Geophysics*, edited by S. H. Ward. pp. 147–189, Soc. of Explor. Geol., Tulsa, Okla., 1990.

Yorkey, T. J., Electrical impedance tomography with piecewise polynomial conductivities, *J. Comput. Phys.*, *91*, 344–360, 1990.

Zhang, J., R. D. MacKie, and T. R. Madden, 3-D resistivity forward modeling and inversion using conjugate gradients, *Geophysics*, *60*, 1313–1325, 1995.

Zhdanov, M. S., and G. V. Keller, The Geoelectrical Methods in Geophysical Exploration, Elsevier Sci., New York, 1994.

D. Gibert, Géosciences Rennes, Université Rennes 1, B15 Campus de Beaulieu, 35042 Rennes cedex, France. (gibert@univ-rennes1.fr)

M. Pessel, Dept. of Geophysics, Colorado School of Mines, 1500 Illinois Street, Golden, CO 80401, USA. (mpessel@mines.edu)